Chemosphere 224 (2019) 910–921

Contents lists available at ScienceDirect

Chemosphere

journal homepage: www.elsevier.com/locate/chemosphere

Fabrication of novel magnetic $MnFe_2O_4$/bio-char composite and heterogeneous photo-Fenton degradation of tetracycline in near neutral pH

Cui Lai [a, b, *], Fanglong Huang [a, b], Guangming Zeng [a, b, **], Danlian Huang [a, b], Lei Qin [a, b], Min Cheng [a, b], Chen Zhang [a, b], Bisheng Li [a, b], Huan Yi [a, b], Shiyu Liu [a, b], Ling Li [a, b], Liang Chen [c]

[a] College of Environmental Science and Engineering, Hunan University, Changsha, Hunan 410082, China
[b] Key Laboratory of Environmental Biology and Pollution Control (Hunan University), Ministry of Education, Changsha, Hunan 410082, China
[c] Faculty of Life Science and Technology, Central South University of Forestry and Technology, Changsha, Hunan, 410004, China

HIGHLIGHTS

- The novel $MnFe_2O_4$/bio-char composite was fabricated as catalyst in photo-Fenton reaction.
- $MnFe_2O_4$/bio-char composite can be easily separated from solution by an external magnetic field.
- 93% of 40 mg L^{-1} TC removal was obtained in 2 h in near neutral pH.
- •OH played the main role in degradation of TC in photo-Fenton reaction.
- $MnFe_2O_4$/bio-char composite showed steady performance in different water body.

GRAPHICAL ABSTRACT

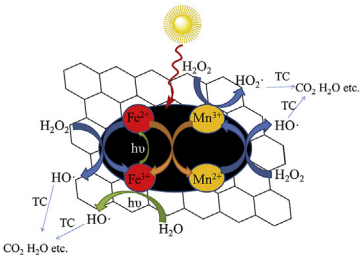

ARTICLE INFO

Article history:
Received 11 September 2018
Received in revised form
25 February 2019
Accepted 28 February 2019
Available online 2 March 2019

Handling Editor: Chang-Ping Yu

Keywords:
Photo-Fenton
Heterogeneous Fenton
Magnetite
Bio-char
Magnetic field

ABSTRACT

Iron-based magnetic materials are deemed to be promising catalysts for various catalytic reactions and can be recovered conveniently by an external magnetic field. $MnFe_2O_4$ nanoparticle and $MnFe_2O_4$/bio-char composite with different bio-char contents were prepared to activate hydrogen peroxide for the degradation of tetracycline (TC). The catalysts were characterized by SEM, BET, XRD, FTIR, VSM and XPS. The results indicated that $MnFe_2O_4$ had a spherical shape and was successfully loaded onto the surface of bio-char. The introduction of bio-char effectively suppressed the aggregation of $MnFe_2O_4$ and drastically increased the specific surface area. Both $MnFe_2O_4$ and $MnFe_2O_4$/bio-char composite can be separated easily by an external magnetic field. Using 1:2 composite as heterogeneous photo-Fenton catalyst obtained a degradation of 95% through visible light irradiation of 40 mg L^{-1}solution at natural pH (pH = 5.5) in the presence of 100 mmol L^{-1} H_2O_2 for 2 h. Free radical quenching experiment and the ESR results confirm that hydroxyl radicals play the main role for TC degradation. XPS measurements show that both Fe and Mn ions simultaneously participate in the activation of H_2O_2. The bio-char not only restrains the aggregation of $MnFe_2O_4$ leading to the improved removal efficiency of TC, but also has side effects by

* Corresponding author. College of Environmental Science and Engineering, Hunan University, Changsha, Hunan, 410082, China.
** Corresponding author. College of Environmental Science and Engineering, Hunan University, Changsha, Hunan 410082, China.
E-mail addresses: laicui@hnu.edu.cn (C. Lai), zgming@hnu.edu.cn (G. Zeng).

https://doi.org/10.1016/j.chemosphere.2019.02.193
0045-6535/Published by Elsevier Ltd.

consuming hydroxyl radicals. By cyclic degradation experiments, the performance of $MnFe_2O_4$/bio-char composite is stable and almost unchanged, and the leaching metal ions of both Fe and Mn are neglectful (both below 0.2 mg L^{-1}). Besides, steady performance of $MnFe_2O_4$/bio-char catalyst to remove TC from tap water and river water has been certified.

Published by Elsevier Ltd.

1. Introduction

Since the discovery of penicillin in 1928, a growing number of antibiotics are used to treat bacterial infections in domestic animals and human body. Many side effects caused by abuse of antibiotics have been shown in our circumstance; bacteria increase resistance in response to antibiotic challenge and reduce the effectiveness of drugs (Qin et al., 2017; Lai et al., 2019). Tetracycline (TC), as one kind of efficient and extensive antibiotics, has been widely used in many fields such as human and livestock feeding (Zhang et al., 2014). Up to now, TC contaminative wastewater has been an ecological risk which is also a threat for human's health (Wang et al., 2018a; Zhang et al., 2018). Therefore, aqueous antibiotic pollution, especially TC pollution is a public concern and needs to be resolved urgently.

Among several wastewater treatment technologies, advanced oxidation process (AOP) as a kind of chemical technology has received broad attention for elimination of various types of refractory pollutants by producing highly reactive species such as hydroxyl radicals (•OH) (Lai et al., 2016; Li et al., 2018; Wang et al., 2018b, 2018c; Zhang et al., 2019; Zhou et al., 2018). Fenton process as one of the most popular advanced oxidation processes which can be operated at normal temperatures and pressures has attracted a lot of interest among researchers. Conventional Fenton process initiates by mixing Fe^{2+} solution with H_2O_2 to produce •OH (Eq. (1)), the generated Fe^{3+} can also catalyze H_2O_2 and produce Fe^{2+} (Eq. (2)). Photo-Fenton reaction is widely concerned because it could accelerate the circulation of Fe (II, III) (Eq. (3)) and produce more reactive radicals (Eqs. (3) and (4)) (Cheng et al., 2016).

$$Fe^{2+} + H_2O_2 \rightarrow Fe^{3+} + HO^- + {\bullet}OH \quad K_1 = 70\ M^{-1}\ s^{-1} \tag{1}$$

$$Fe^{3+} + H_2O_2 \rightarrow Fe^{2+} + H^+ + HO_2{\bullet} \quad K_2 = 0.001\text{–}0.1\ M^{-1}\ s^{-1} \tag{2}$$

$$Fe^{3+} + H_2O + h\upsilon \rightarrow Fe^{2+} + {\bullet}OH + H^+ \tag{3}$$

$$H_2O_2 + h\upsilon \rightarrow 2{\bullet}OH \tag{4}$$

However, the traditional homogeneous Fenton reactions have some disadvantages such as strict pH range around 3, high cost for neutralizing effluent after treatment and generation of iron sludge after neutralization. To overcome these drawbacks in conventional Fenton processes, much effort has been made on the development of heterogeneous Fenton-like processes in which solid iron-based catalysts were used instead of soluble iron salts (Cheng et al., 2017). Various natural iron minerals and iron oxide were applied to the treatment of refractory organic contaminants in a wider pH range (Xu et al., 2009; Rusevova et al., 2012; Hou et al., 2016; Villegas- Guzman et al., 2017). But pure metallic oxide catalysts are found to have some disadvantages that hinder practical application such as poor stability, relative inert activity and recyclability.

In recent years, another metal species, manganese, which possesses a similar role as iron to present heterogeneous catalytic functions, has triggered considerable research interest (Li et al., 2015; Duan et al., 2016; Zhou et al., 2016; Wan and Wang, 2017). Mn and Fe ions are believed to present heterogeneous catalytic functions in the $MnFe_2O_4/H_2O_2$ system and the $MnFe_2O_4$ nanoparticles are quite stable during the catalytic process for its specific spinel crystal structure (Goodarz Naseri et al., 2011; Galindo et al., 2014). In addition, The Fe and Mn elements are abundant and environmentally friendly, which can be obtained by metallurgical waste water and steel slag. Furthermore, manganese ferrite ($MnFe_2O_4$) nanoparticles are magnetic materials which can be easily separated from aqueous solutions by external magnetic fields, providing an attractive and cost-effective method for practical operation (Mazarío et al., 2016; Ueda Yamaguchi et al., 2016). Nevertheless, nanoparticles especially magnetic nanoparticles always tend to be aggregated due to its inherent high surface energy and strong interparticle magnetic interactions, which inevitably causes negative impact on the catalytic activity of catalyst (Tuček et al., 2014; Xiong et al., 2017).

Iron based heterogeneous Fenton-like catalysts loaded on solid supports such as silica- (Mazilu et al., 2017; Jinisha et al., 2018), clay- (Feng et al., 2003; Timofeeva et al., 2009) and carbon-supported materials (Huang et al., 2018; Wang et al., 2017; Yi et al., 2018) were extensively studied due to the stability, low toxicity and wide availability (Qian et al., 2018). Carbonaceous materials have showed great potential in environmental remediation due to their excellent chemical and thermal stability, high surface area with versatile surface functional groups and low cost. Graphene oxide and carbon nanotube are the most popular one-atom thick carbon materials that have attracted extensive attention (Zhou et al., 2016; Guo et al., 2017; Jiang et al., 2017; Liu et al., 2017), but the high economic costs hinders their further development. Recently, bio-char has aroused a fever of interest among researchers for its low-cost economies, wide availability and abundant surface functional groups that could facilitate the catalytic effect (Yan et al., 2015; Huang et al., 2019; Dong et al., 2017; Wang et al., 2018d).

$MnFe_2O_4$/bio-char composite has not been previously studied as double-effect heterogeneous photo-Fenton catalysts for degradation of TC. In this work, we prepare a $MnFe_2O_4$/bio-char composite and evaluate its photo-Fenton catalytic activities during TC decomposition under visible light irradiation in the presence of hydrogen peroxide (H_2O_2). The influence of different mass ratio between $MnFe_2O_4$ and bio-char, pH, H_2O_2 concentration and catalyst dosage are discussed. The mechanism and the stability of catalyst are also probed.

2. Materials and methods

2.1. Chemicals

Ferric chloride hexahydrate ($FeCl_3 \cdot 6H_2O$), manganese dichloride tetrahydrate ($MnCl_2 \cdot 4H_2O$), ammonium hydroxide ($NH_3 \cdot H_2O$), sodium hydroxide (NaOH), hydrochloric acid (HCl, 36%) and hydrogen peroxide (H_2O_2) were purchased from Sinopharm Chemical Reagent, China. All of these chemicals were of analytical grade without further purification. Ultrapure water (18.25 MΩ, Milli-Q Millipore) was used in all experiments.

2.2. Preparation of $MnFe_2O_4$/bio-char composite

Pine needles were collected from the campus of Hunan University, China. After removing impurities attached on the surface of raw materials using ultrapure water several times, pine needles were dried at 105 °C to a constant weight and grinded by a cutting mill before passing through a 100-mesh sieve. Then the ground raw materials were pyrolyzed with an OTF-1200X-L tubular furnace at 500 °C for 2 h with a heating rate of 10 °C/min under a constant N_2 flow rate. The obtained bio-chars were stored in an airtight desiccator prior to use.

The $MnFe_2O_4$/bio-char composite was synthesized through a co-precipitation method. The synthesis process of $MnFe_2O_4$/bio-char was described as follows: $MnCl_2 \cdot 4H_2O$ (0.4948 g, 0.0025 mol) and $FeCl_3 \cdot 6H_2O$ (1.3516 g, 0.005 mol) were separately dissolved in 40.0 mL of deionized water. A certain amount of bio-char was added into above mixed solutions and dispersed under ultrasound for 30 min. Then 30 mL of 3 M $NH_3 \cdot H_2O$ was added drop-wise into the suspensions in a magnetic stirring water bath for 1 h at 80 °C. After reaction, the solution was cooled down to a room temperature and the achieved $MnFe_2O_4$/bio-char composite was centrifugally separated and washed with ethanol and ultrapure water until the filtrate pH reached the neutral region. Then they were dried in an oven at 60 °C for 24 h and stored in a sealed container for the characterization and experiments. $MnFe_2O_4$/bio-char composites with different $MnFe_2O_4$ to bio-char mass ratios were also prepared by changing the mass of bio-char dispersed in the solution.

2.3. Characterization

The morphology of $MnFe_2O_4$/bio-char composite was obtained by a scanning electron microscope (SEM, Sirion 200) equipped with energy dispersive spectrometer (EDS, INCA X-Act). The samples were characterized by X-ray Diffraction (XRD) using a D/max-2400 diffraction meter. Diffraction patterns were acquired between 10° and 80° with 8° min^{-1} step using an X-ray source emitting Cu-Kα radiation with a wavelength of 0.154 nm at a tube voltage of 40 kV and a tube current of 40 mA. The Brunauer-Emmett-Teller (BET) specific surface areas of typical products were performed at 77 K in an AUTOSORB-1-MP system. Fourier transform infrared (FT-IR) spectrophotometer (Spectrum BX; PerkinElmer Ltd., USA) was used to characterize group vibrations at an optical resolution of 4 cm^{-1}. The mulls of $MnFe_2O_4$/bio-char composite were supported by a KBr plate. X-ray photoelectron spectrometer (XPS) with an XSAM 800 apparatus was used to characterize the valence states of Fe, Mn and C in the $MnFe_2O_4$/bio-char composite before and after irradiation to elucidate the relevant reaction mechanism.

2.4. Experimental procedure

The adsorption and catalytic degradation experiments were carried out in a 250 mL beaker in a thermostatic water bath magnetic stirrer. TC adsorption by the prepared materials was tested before examining TC degradation in the $MnFe_2O_4$/bio-char/H_2O_2 system. After shaking for 1 h in the dark, equilibrium was established, and the results were shown in Fig. S1. TC removal efficiency increased rapidly in 30 min, while it barely grew in later 30 min. Based on this result, the time for adding H_2O_2 to initiate catalytic reaction was selected to be 30 min after the addition of catalyst in solution. Typically , 0.05 g catalyst was introduced into 100 mL volume of 40 mg L^{-1} TC solution with stirring to maintain a uniform suspension. After reaching adsorption/desorption equilibrium, a certain amount of H_2O_2 was added to trigger the catalytic reaction with the visible light irradiation under natural pH (pH = 5.5). 300 W xenon lamp with a 420 nm cutoff filter was used as a simulated solar light source. The distance between irradiation source and the surface of the solution is 15 cm and the light intensity was determined as 155 mW cm^{-2}. The pH was adjusted with dilute 0.1 M HCl or 0.1 M NaOH while investigating pH on the effects of tetracycline removal. All experiments were operated at constant temperature of 20 °C and stirred at 300 rpm. At the same interval, the samples were withdrawn from the beaker and filtered through Organic filter head with 0.22 μm. The UV–Vis absorbance of the filtrate was measured on a UV–Vis spectrophotometer at 357 nm corresponding to the maximum absorbance of tetracycline. The degradation efficiency was calculated by the following formula:

$$\text{TC degradation efficiency} = (C_0\text{-}C_t)/C_0 \times 100\% \quad (5)$$

where C_0 and C_t represents the concentration of TC at initial and desired time intervals, respectively. The residual concentration of H_2O_2 was followed using the metavanadate spectrophotometric method at 459 nm (Nogueira et al., 2005). Total organic carbon (TOC) of samples was determined with a Shimadzu 5000 TOC analyzer. The intermediates analysis was performed by an ultra-high-performance liquid chromatography mass spectrometer (UPLC-MS, Agilent 1290/6460, Triple Quad MS, USA) system equipped with a Symmetry C18 column (50 mm × 2.1 mm × 5 mm). Iron and manganese concentration in the solution after the reaction were measured by flameless atomic absorption spectrometer (AAS, PEAA700, Perkin Elmer, USA).

3. Results and discussion

3.1. Characterization of catalysts

Morphological structure of pure $MnFe_2O_4$ and $MnFe_2O_4$/bio-char composite with 1:2 mass radio has been observed by SEM as shown in Fig. S2a–d. The pure $MnFe_2O_4$ which was prepared in the absence of bio-char showed spherical nanoparticles with particle size about 40 nm (Fig. S2a–b), but the cluster size of the $MnFe_2O_4$ microspheres caused by the aggregation of plenty of smaller $MnFe_2O_4$ nanoparticles was estimated between 100 and 300 nm. The bio-char as a support is expected to prevent the aggregation of the small nanoparticles and enlarge the specific surface area by the interaction between the pure $MnFe_2O_4$ nanoparticles and bio-char due to the abundant oxygen-containing functional groups (Zhou et al., 2016). As a contrast in Fig. S2c and d, the $MnFe_2O_4$ spherical particles were entirely anchored on the bio-char rough surfaces. With the assistance of EDS analysis in selected area from Fig. S2d, the composition of the as-prepared materials was confirmed with the presence of Mn, Fe, O and C, which can prove that $MnFe_2O_4$ nanoparticles are successfully attached on the surface of bio-char.

N_2 adsorption–desorption isotherms (Fig. S3a) were measured and displayed type IV curve and H3 hysteresis loop according to IUPAC (International Union of Pure and Applied Chemistry) classification. This behavior shows the predominance of mesopores. Type H3 hysteresis indicates the random distribution of pores and the interconnection of pores. BET surface areas (shown in Table 1) of $MnFe_2O_4$ and $MnFe_2O_4$/bio-char composite with 1:2 mass ratio are 75.25 and 121.45 $m^2 g^{-1}$, respectively. In addition, the pore size distributions are presented in Fig. S3b; the composite showed more concentrated pore size distribution than pure $MnFe_2O_4$ with mean values of 3.17 and 4.12 nm, respectively. S_{BET} value increased and the average pore size decreased after introducing bio-char as support, because the abundant oxygen-containing functional groups on the surface of bio-char provide crystal growth site and effectively suppress the agglomeration of $MnFe_2O_4$ and make it disperse uniformly (Nguyen et al., 2011; Juang et al., 2018).

Table 1
BET and VSM parameters.

samples	Surface area(m^2 g^{-1})	Pore volume(cm^3 g^{-1})	Pore size(nm)	Ms(emu g^{-1})	Mr(emu g^{-1})	Hc(Oe)
$MnFe_2O_4$	75.2521	0.202182	4.1198	47.22	1.2	10.2
1:2 composite	121.4536	0.218390	3.1730	11.76	0.41	13.5

The X-ray diffraction patterns of pure $MnFe_2O_4$ and $MnFe_2O_4$/bio-char composite with 1:2 mass ratio were shown in Fig. 1a. The diffraction peaks obtained matched well with cubic $MnFe_2O_4$ (JCPDS Card No. 73-1964, space group: Fd3m a = 8.52 Å). Peaks observed at 2θ of 17.84°, 29.58°,34.88°, 36.42°, 42.52°, 52.78°, 56.22°, 61.74° and 72.80° represent Bragg reflections from the (111), (220), (311), (222), (400), (422), (511), (440) and (533) planes, respectively. The average diameter of pure nanoparticles was calculated by Debye–Scherrer equation D = K λ/(W cosθ) based on the (311) lattice plane. In the equation, W is the width of the diffraction peak at its half height, K is the so-called shape factor (usually approximately 0.89), and λ is the wavelength of the X-ray source which is 0.154 nm in this experiment. The diameter based on the equation is estimated about 42 nm for pure $MnFe_2O_4$, which is in accordance with the SEM results. As for $MnFe_2O_4$/bio-char hybrid material, the estimated diameter is about 24 nm, which is similar to the $MnFe_2O_4$/graphene oxide (Ueda Yamaguchi et al., 2016). The decrease in the size of $MnFe_2O_4$ nanoparticles in composite may be attributed to the fact that one side of the nanoparticles growth was blocked when grown in situ onto the surface of the bio-char.

FT-IR spectra and spectroscopic assignment of the $MnFe_2O_4$/bio-char composite and pristine bio-char are shown in Fig. 1b. The absorption bands of Mn–O and Fe–O bonds from $MnFe_2O_4$/bio-char composite appear at 459 and 580 cm^{-1}, respectively. The peaks at 459 and 580 cm^{-1} severally confirm the formation of metal-oxygen bonds at octahedral sites and tetrahedral sites of the spinel structure, which indicates that the manganese ferrite was well attached on the surface of the bio-char which can be seen in Fig. S2c coating irregular biochar (Zhou et al., 2016). The pristine bio-char had broad bands at 3450-3400 cm^{-1}, due to the vibration of the –OH groups in the presence of cellulose (Son et al., 2018). But as a contrast, the composite had higher peaks at 3450-3400 cm^{-1}, which indicates abundant metal-OH groups appear on the surface of composite. The obvious band around 1640 cm^{-1} corresponding to the C=C bonds from bio-char appeared which indicates high carbon content and aromatization in the bio-char. Other obvious peaks around 1450-1400 cm^{-1} were assigned to C=O stretching probably due to carboxylic acid on the surface of bio-char. The peaks between 1300 and 1000 cm^{-1} ascribed to C–O stretching from bio-char decreased after introducing metal oxide, this phenomenon could be caused by the formation of Metal–*O*–C bonds in the surface of composites, which was explored by other researchers (Zhou et al., 2012; Zubir et al., 2014). The functional groups with versatile abilities on the composite surface play an important role in heterogeneous catalysis by offering active site.

Vibrating sample magnetometer (VSM) was applied to analyze the magnetization of $MnFe_2O_4$ and $MnFe_2O_4$/bio-char composite and the magnetic properties are shown in Fig. 1c and Table 1. The saturation magnetization of $MnFe_2O_4$ and $MnFe_2O_4$/bio-char composite were measured to be 47.22 and 11.75 emu g^{-1}, respectively. This indicated that large amount of $MnFe_2O_4$ was successfully loaded on the surface of bio-char. The decrease of saturation magnetization could result from the existence of bio-char and the smaller size of magnetic particles. So the $MnFe_2O_4$/bio-char composite could be easily separated by exterior magnetic field. Besides, the optical properties of prepared samples were analyzed by UV–Vis DRS spectra in Fig. S4. Obviously, both the $MnFe_2O_4$ and the

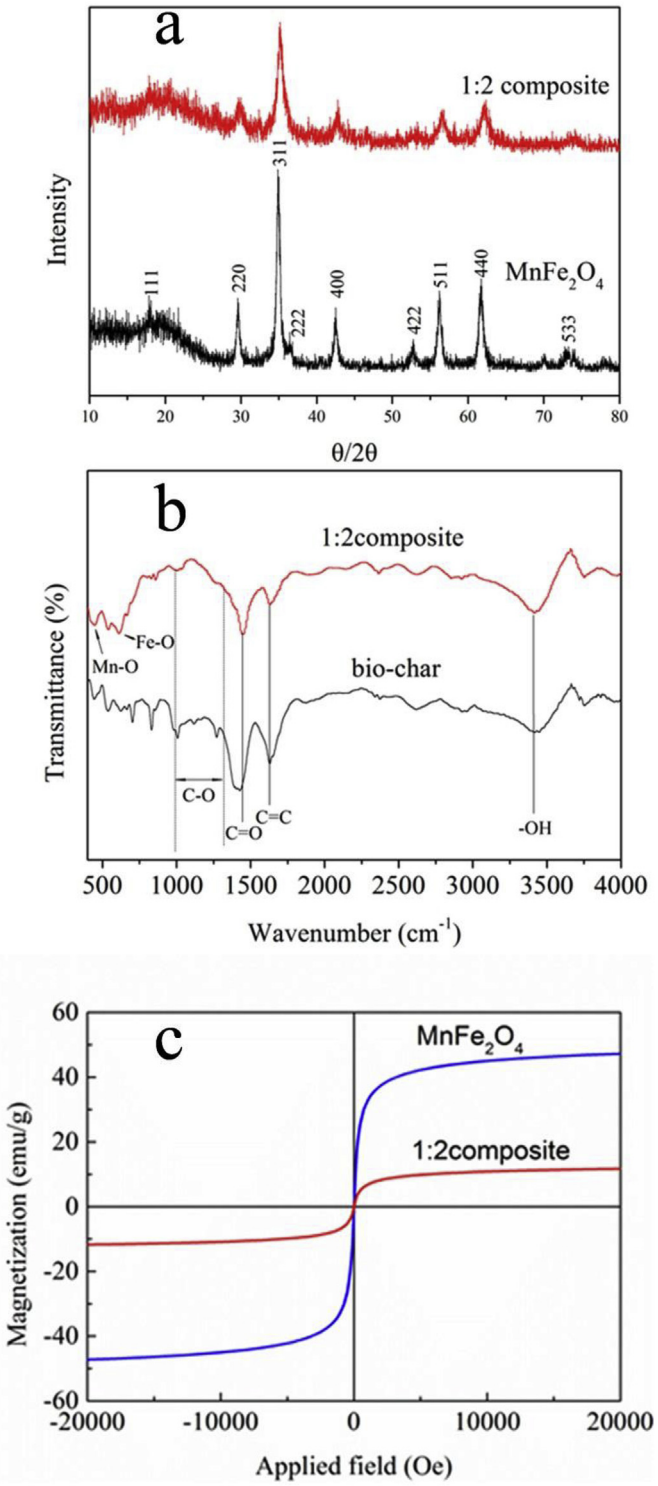

Fig. 1. XRD patterns (a) of $MnFe_2O_4$ and $MnFe_2O_4$/bio-char composite with 1:2 mass ratio, FT-IR spectra (b) of bio-char and $MnFe_2O_4$/bio-char composite with 1:2 mass ratio and Hysteresis loops (c) of $MnFe_2O_4$ and $MnFe_2O_4$/bio-char composite with 1:2 mass ratio.

1:2 composite possessed UV–Vis light absorption ability. After bio-char was coated with $MnFe_2O_4$, 1:2 composite exhibited a broad absorption in UV to Vis region which guaranteed the prepared materials could be activated under visible light irradiation.

3.2. Catalytic degradation of TC by $MnFe_2O_4$/bio-char composites with different mass ratio

$MnFe_2O_4$ and $MnFe_2O_4$/bio-char composites with different mass ratio were applied for the catalytic degradation of TC under visible light irradiation in the presence of H_2O_2 at natural pH. The effect of mass ratio between $MnFe_2O_4$ and bio-char on the activity of catalysts was shown in Fig. 2a. As we can see, the removal efficiency of 3:1, 1:1, 1:2 and 1:3 mass ratios between $MnFe_2O_4$ and bio-char was 90%, 92%, 95% and 89% in 120 min, respectively. With the bio-char content increased in the composite, the removal efficiency grew in the early stage and then decreased slightly. The experimental result is similar to nFe_3O_4/bio-char (Ouyang et al., 2017). More active sites on the surface of catalyst are available with the increased surface area and pore volume while the bio-char content increased in some extent. However, an excessive content of bio-char could block the active sites leading to reduced efficiency. From the above discussion, the mass ratio between $MnFe_2O_4$ and bio-char at 1:2 shows optimal removal efficiency in the degradation of TC. Thus, $MnFe_2O_4$/bio-char composite with a mass ratio of 1:2 was selected in the following experiment.

3.3. The degradation performance of TC in different reaction systems

The degradation curves of TC under different experiment conditions are presented in Fig. 2b. H_2O_2 alone was unable to significantly degrade TC under visible light irradiation in 120 min, the degradation efficiency was negligible. The photolysis of TC caused little removal efficiency, proving the photostability of TC. Bare $MnFe_2O_4$ resulted in TC degradation efficiency of 72% after 120 min reaction. Compared with $MnFe_2O_4$/bio-char composite, the relatively lower TC degradation efficiency under visible light irradiation might be due to the aggregation of $MnFe_2O_4$ particles with a relative small S_{BET} value of 75.25 $m^2 g^{-1}$. The degradation efficiency of TC was 75% within 120 min by heterogeneous Fenton oxidation of $MnFe_2O_4$/bio-char composite in dark, nevertheless, the degradation efficiency greatly improved to be 93% under visible light irradiation within 90 min. In order to further investigate the effects of light on catalytic effects, we also test the TOC decrease and tendency of H_2O_2 consumption on the Fenton and photo-Fenton process. As shown in Table 2, not only TC removal efficiency increased from 75% to 93%, TOC removal efficiency grew from 10% to 37.5%, which means more intermediates produced in early stage had been mineralized into inorganic ions in photo-Fenton system. The pseudo-first order reaction kinetics constant of H_2O_2 consumption changed from 0.0314 min^{-1} to 0.0386 min^{-1} after irradiation with visible light (Fig. S5a), which proves improved catalytic performance of catalyst towards H_2O_2 consumption with the assistance of visible light. Besides, TC removal and H_2O_2 consumption are compared in Fig. S5b. As we can see, in the first 30 min after adding H_2O_2, both TC removal rate and H_2O_2 consumption rate are fast, which means predominant reaction is between the active radical and TC, finally leading the transformation of TC into intermediates. From 30 min to 60 min, TC removal rate declines sharply while H_2O_2 consumption rate still maintains at a relatively higher level, which indicates that both TC and intermediates react with the active radicals and eventually leads both TC removal and TOC decrease. In the later 60 min, the TC concentration is nearly unchanged but H_2O_2 concentration still drops slowly, which suggests the main reaction is between intermediates and the active radical. The enhanced catalytic performance under visible light irradiation could be due to acceleration of the Fe (III)/Fe (II) circulation (eq. (3)) (Liu et al., 2018). Therefore, $MnFe_2O_4$/bio-char composite is a promising photo-Fenton catalyst for TC removal.

Table 2
The index in different heterogenous Fenton-like system.

System	Time (min)	TC degradation efficiency (%)	TOC removal (%)	First-order reaction rate constant of H_2O_2 consumption (min^{-1})
Fenton	120	75	10	0.0314
Photo-Fenton	120	93	37.5	0.0386

3.4. Effects of H_2O_2 concentration, catalyst dosage and pH on tetracycline removal

In order to assess the effect of H_2O_2 concentration on the degradation efficiency of tetracycline, the dosage of H_2O_2 ranging from 50 to 200 mM was added in the experiments. As we can see in Fig. 3a, The removal efficiency increased rapidly from 79% to 92% with the increasing dosage of H_2O_2 from 50 to 100 mM. Nevertheless, while the dosage of H_2O_2 increased from 100 to 200 mM, the removal efficiency barely grew. This is because the increasing amount of H_2O_2 within range of 50–100 mM reacted with the redundant active sites on the surface of the catalysts and generated more •OH, However, the increase in TC removal was not obvious with further increasing the dosage of H_2O_2 from 100 to 200 mM. To

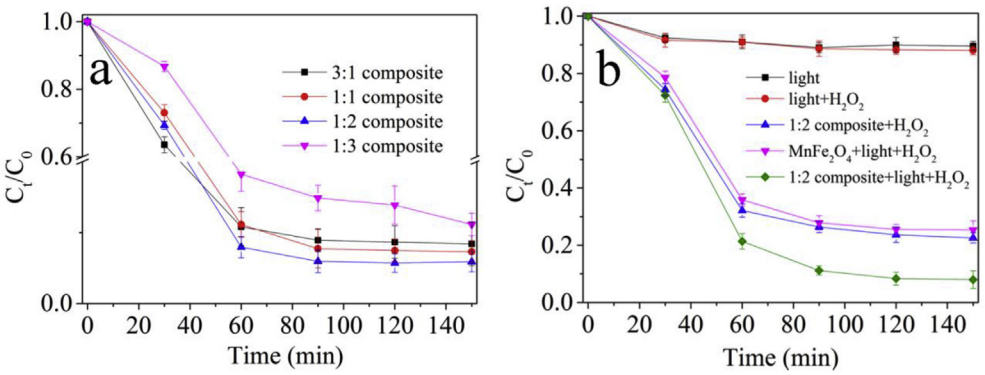

Fig. 2. Photo-Fenton degradation of TC by different mass ratio $MnFe_2O_4$/bio-char composite (a) and the degradation of TC in different operation systems (b). Reaction conditions: TC concentration = 40 mg L^{-1}, H_2O_2 concentration = 100 mmol L^{-1}, catalyst loading = 0.5 g L^{-1}, Temperature = 20 °C under natural pH.

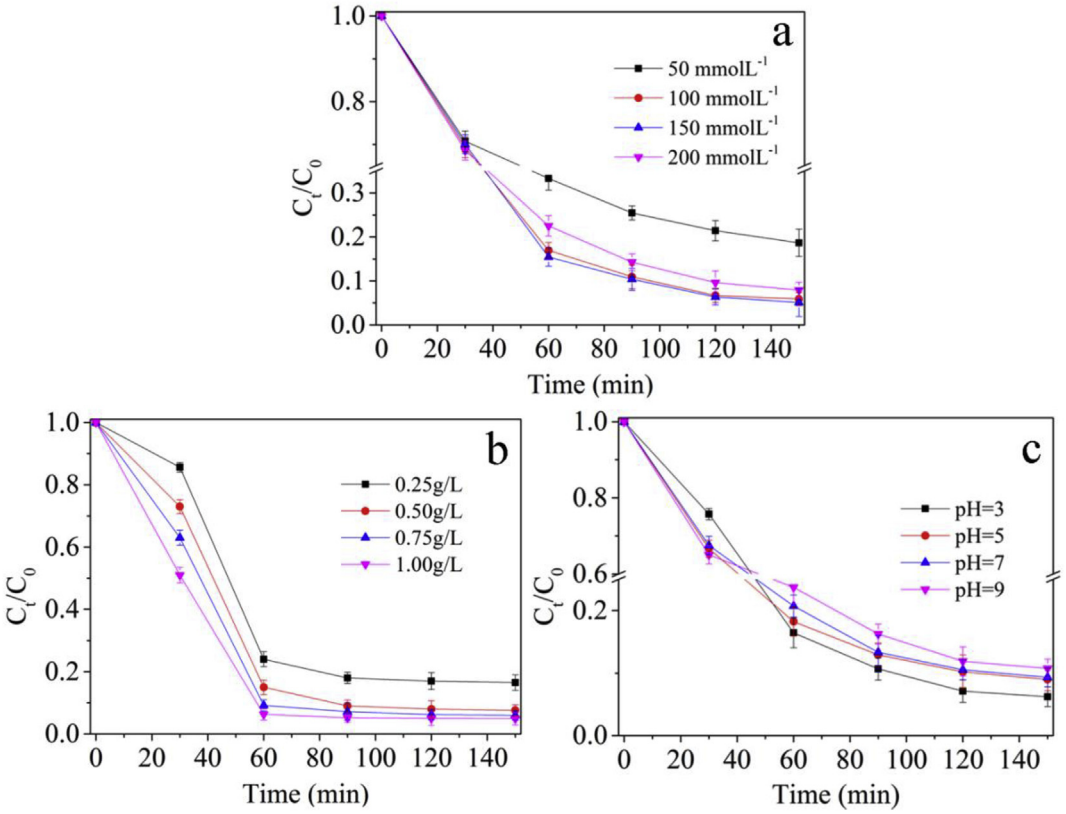

Fig. 3. Photo-Fenton degradation of TC in different H_2O_2 concentration (a), catalyst loading (b) and initial pH (c). (Reaction conditions: TC concentration = 40 mg L^{-1}, catalyst loading = 0.5 g L^{-1}, H_2O_2 concentration = 100 mmol L^{-1}, Temperature = 20 °C under natural pH, except for tested condition).

some extent, the residual H_2O_2 with no redundant active sites to react with could compete with TC for •OH (Eq. (6) and (7)) (Guo et al., 2017; Cheng et al., 2018b).

$$H_2O_2 + {\bullet}OH \rightarrow HO_2{\bullet} + H_2O \quad (6)$$

$$HO_2{\bullet} + {\bullet}OH \rightarrow O_2 + H_2O \quad (7)$$

The effect of catalyst dosage on the removal efficiency of tetracycline was tested later. From the results in Fig. 3b, the removal efficiency grew from 86% to 95% along with the catalyst dosage increasing from 0.025 to 0.5 g L^{-1} in 120 min. Maybe more catalyst will offer more active sites to react with H_2O_2, hence accelerate the generation of •OH and improve the removal efficiency. However, with the catalyst further increasing, ignorable increase was observed. This is because excess Fe ions on the surface might lead the undesirable consumption of active radicals and reduce the available active radicals that should react with target pollutants (eq. (8)) (Zhong et al., 2012). Furthermore, excessive catalyst weakens the penetration of light and reduces the available radiation (Iurascu et al., 2009). The two reasons counteracted the advantage of more active sites provided by more catalyst.

$$Fe^{2+} + {\bullet}OH \rightarrow Fe^{3+} + OH^- \quad (8)$$

As we all know, solution pH can remarkably influence the catalytic effect in the Fenton system. (Huang et al., 2019). The effect of initial pH on the removal efficiency of TC was determined. As shown in Fig. 3c, All of the removal efficiencies were above 90% with the initial pH ranging from 3 to 9. But the removal efficiencies are relatively higher in pH 3. H_2O_2 consumption was also tested under different pH values in Fig. S6. The hydrogen peroxide consumptions were 26%, 76%, 81% and 83% under pH 3, 5, 7, 9, respectively. H_2O_2 consumption was lower under pH 3 than other conditions. A large number of H_2O_2 are consumed in Eq. (2) or break down into water and oxygen under near neutral condition (pH = 5-9) and basic conditions. As for basic conditions around 9, the relatively lower degradation efficiency could be caused by the fact that hydroxyl radical has a redox potential of +2.8 V in acidic media and +1.5 V in basic media (Wang and Xu, 2012). The degradation efficiency in pH 5 and pH 7 were similar, proving that the catalytic performance is efficient in near neutral pH conditions. As we all know, the most disadvantage in classic Fenton system is the requirement of acidic conditions, in which the solution pH is around 3, which increased costs and caused secondary pollution of iron sludge. The surface Fenton system of most iron oxide in near neutral pH was passivated. In this system, Mn elements maybe play an important role in catalyzing H_2O_2 and producing active radicals in near neutral pH condition. In other ways, the smaller size of $MnFe_2O_4$ nanoparticles dispersed on the surface of bio-char were able to provide more active sites and improved catalytic performance in near neutral pH conditions. So, in this work, combination of bio-char and $MnFe_2O_4$ provides potential candidate in Fenton system to treat organic contaminants.

3.5. Inorganic ions effects on the TC degradation

As we all know, inorganic ions in water may have impacts on the degradation process. So some typical anions such as Cl^-, SO_4^{2-}, CO_3^{2-} and PO_4^{3-} and cations such as Mg^{2+} and Ca^{2+} were added to the solution to probe their influence on the photo-Fenton reactions. From Fig. S7, we can see that Cl^- and SO_4^{2-} show little impact in this

reaction, but the presence of CO_3^{2-} and PO_4^{3-} significantly improve the degradation rates. According to previous reports, the scavenging effect of carbonate ions on hydroxyl radical may suppress the degradation process (Xiao et al., 2008). However, carbonate ions facilitates the degradation of TC in photo-Fenton reactions. It could be that carbonate ions as well as phosphate in solution could prevent ferrous ion from oxidizing by hydroxyl radicals (eq. (8)) and render the Fe (III/II) circulation in near neutral pH. As for cations Mg^{2+} and Ca^{2+}, we know that Mg^{2+} and Ca^{2+} could react with TC to form stable metal complex and the degradation processes were hindered for the decline of available TC adsorbed on the surface of solid catalyst (Tongaree et al., 1999). From the results in Fig. S7, Mg^{2+} cations showed an obviously inhibitory effect than Ca^{2+} cations. It was reported that stability constants for Mg^{2+} and Ca^{2+} to TC complexes were roughly equal (Chen and Huang, 2011). So, we can not only consider the complexation between metal ion and TC. The combination of metal ion and TC could change surface charge of TC and affect the adsorption between catalysts and TC. As shown in Fig. S7, the addition of Mg^{2+} cations caused decreased adsorption capacity of catalyst on TC. So, both complexation and the adsorption account for the decreased degradation efficiency caused by cations of Mg^{2+} and Ca^{2+}.

3.6. Intermediate product analysis

The main intermediate products were identified by UPLC-MS technology. The TC degradation process was provided in Fig. S8, as we can see, the concentration of tetracycline decreased gradually with time and the peak of TC almost disappeared in 120 min. The tested molecular weights and possible molecular structure were presented in Fig. 4. The main intermediate product molecular weights were 340, 417, 475, 397, 459, and 446 respectively, which has appeared in nearly 5.147 min, 4.217 min, 4.487 min, 5.306 min, 4.784 min, and 4.403 min. And the degradation pathway could be divided into two parts. First (Pathway 1), N-demethylation occurred at C4 position and generated 417 products. As described elsewhere; the N-demethylation should proceed step by step at C4 position, generating 4-demethyltetracycline (433) and 4-dedimethyltetracycline (417), respectively (Ji et al., 2016). But the intermediate product with *m/z* of 433 was not detected, which could be caused by quick reaction of N-demethylation during the H_2O_2 oxidation system (Chen et al., 2017). Then the amino group at C4 position was further oxidized and produces 397 products with dehydration at C6 position. On the other hand (Pathway 2), TC was oxidized at C5 position generating carbonyl groups (459 products).

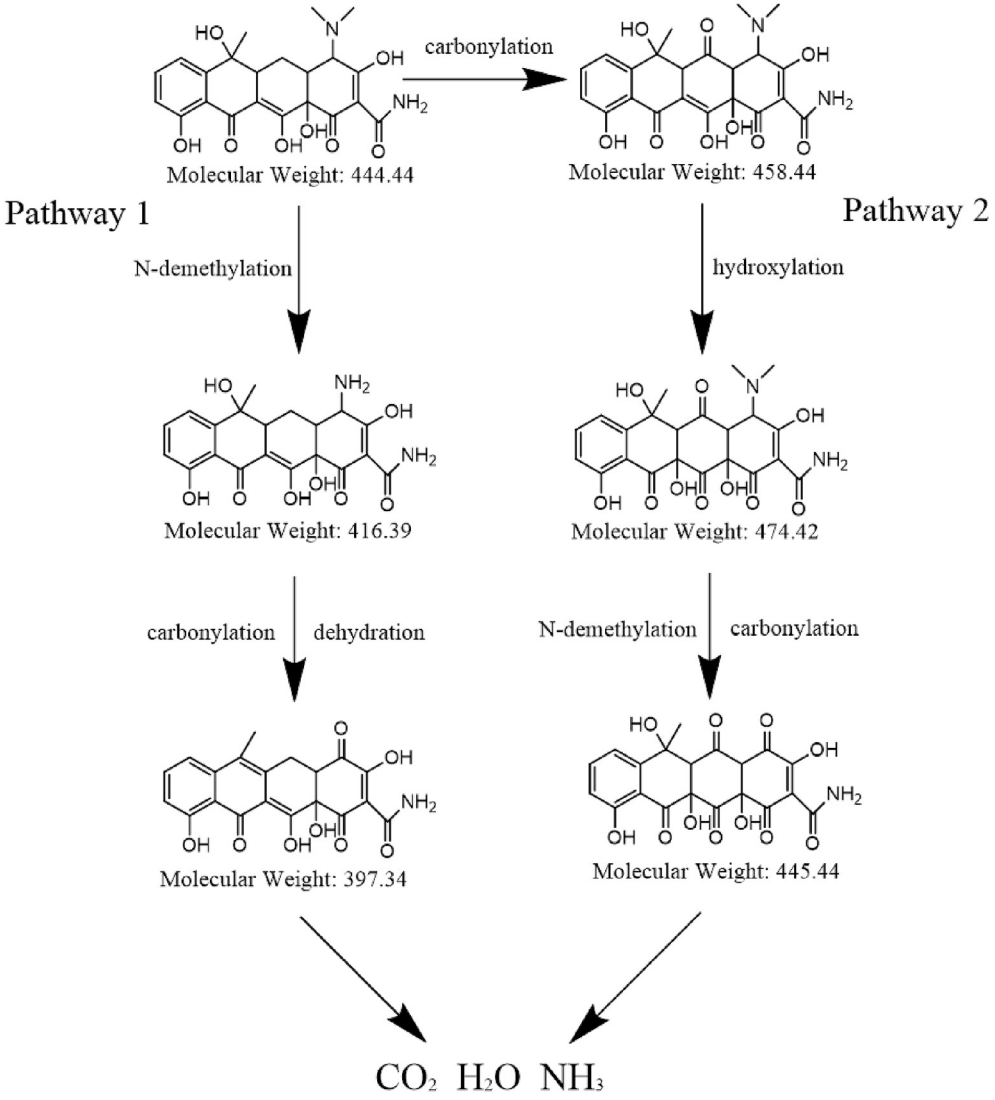

Fig. 4. The degradation pathway of TC by photo-Fenton process.

Then the 459 products was introduced a hydroxyl group at C11a position leading to the generation of 475 products. 475 products was next proceeding N-demethylation and introduced carbonyl groups at C4 position (446 products). Both 397 products and 446 products can be further decomposed into small molecular substances such as main intermediate products with molecular weights of 340. Fig. S9 has provided mass spectrum in different time, with the extension of time, some faint peaks caused by the intermediate products appeared. This phenomenon shows that the generated intermediate products were further degraded into low molecular weight organic matter or even CO_2 and H_2O.

3.7. The identification of free radicals in oxidation experiments

It has been obtained that the catalytic oxidation of contaminants is owing to the generation of free radicals by activating H_2O_2 in the Fenton system (Cheng et al., 2018a). So, free radical trapping experiment is necessary to identify the difference of contributions between different free radicals. In this study, *tert*-butyl alcohol (TBA) was utilized for hydroxyl radical (•OH) scavenger and *p*-benzoquinone (BQ) was used for superoxide radical ($\bullet O_2^-$) scavenger. As shown in Fig. 5a, a slight decline of the TC removal efficiency was obtained with the addition of BQ, proving that $\bullet O_2^-$ played a weaker role in TC removal. As a contrast, significant inhibition effect was observed after adding TBA. The removal efficiency decreased from 93% to 52% in 150 min in the presence of 50 mM TBA, confirming the dominant role of •OH in the Fenton system. In order to further investigate the contribution of •OH and $\bullet O_2^-$, ESR analysis with DMPO as the spin-trapping agent was tested in Fig. 5b and c. As we can see, with the time increasing from 0 to 10 min, the signal of the DMPO-•OH (four characteristic peaks, 1:2:2:1) appeared and increased, proving that the •OH was generated in this heterogeneous photo Fenton-like system. Similar to •OH, the signal of DMPO-$\bullet O_2^-$ adduct also appeared and increased, which indicates that $\bullet O_2^-$ also takes part in the degradation of TC in this heterogeneous photo Fenton-like system. However, the peak intensities of DMPO-•OH were more obvious compared with that of DMPO-$\bullet O_2^-$. So, the ESR results were consistent with free radical trapping experiment. In this heterogeneous photo Fenton-like system, •OH played main role in oxidizing TC into intermediates and further mineralizing into inorganic salts and water. $\bullet O_2^-$ also partially contributed the degradation of TC.

3.8. The catalytic mechanism of H_2O_2 by $MnFe_2O_4$/bio-char composite

To further verify the chemical composition and surface characteristics of the as-synthesized $MnFe_2O_4$/bio-char composite, XPS measurements were recorded. Distinct peaks due the elements Mn, Fe, C, and O are evident in the wide scan XPS survey of $MnFe_2O_4$/bio-char composite (Fig. 6a). The peaks obtained at 285, 530, 642 and 711 eV correspond to the C 1s in sp2 carbon, O 1s of oxygen, Mn 2p, and Fe 2p species respectively.

Fe (II, III) ion cycling is regarded as the driving force to produce hydroxyl radicals, which can degrade various organic contaminants. In Fig. 6b, the Fe 2p spectra show two main peaks at 711.15 and 724.68 eV, which may be assigned to Fe $2p^{3/2}$ and Fe $2p^{1/2}$, respectively. A satellite peak is obvious at the Eb of around

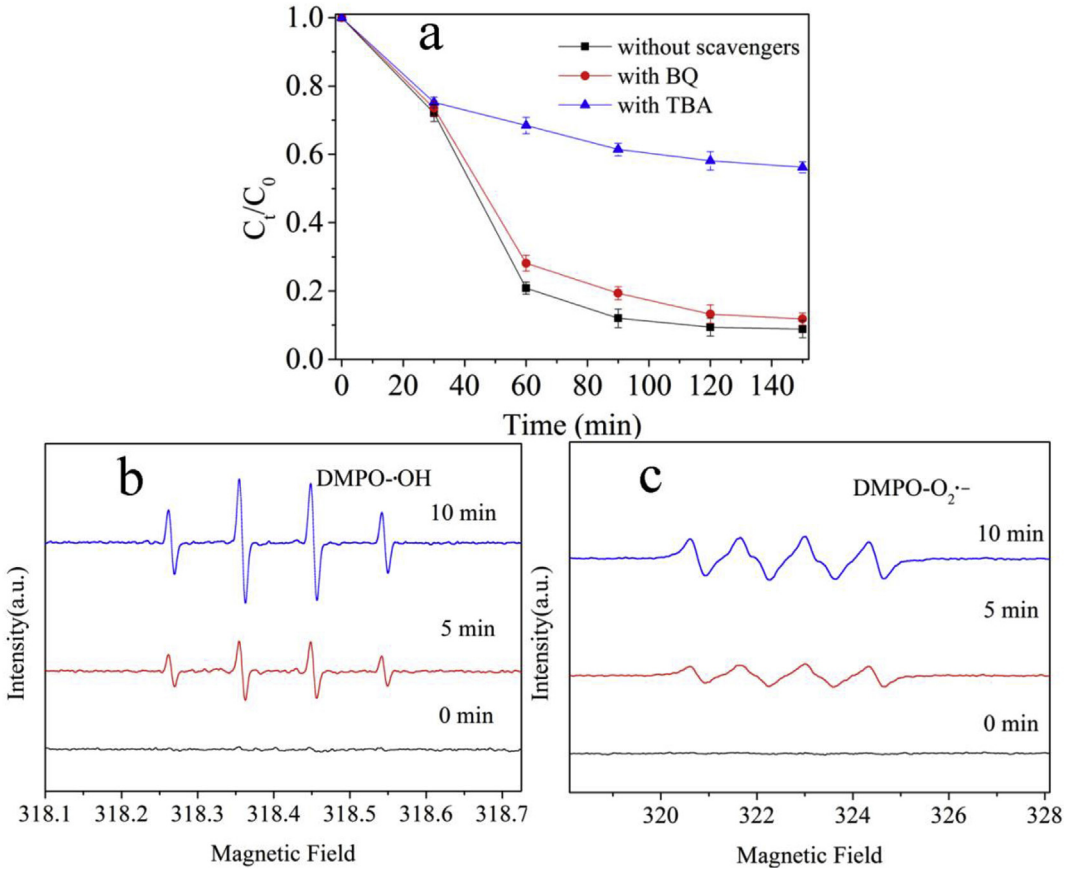

Fig. 5. Effect of radical scavengers on photo-Fenton degradation of TC (a) and ESR spectra of DMPO-•OH (b) and DMPO-$O_2^{\bullet-}$ (c). Scavenger reaction conditions: Scavenger concentration = 50 mmol L^{-1}, TC concentration = 40 mg L^{-1}, H_2O_2 concentration = 100 mmol L^{-1}, catalyst loading = 0.5 g L^{-1}, Temperature = 20 °C under natural pH.

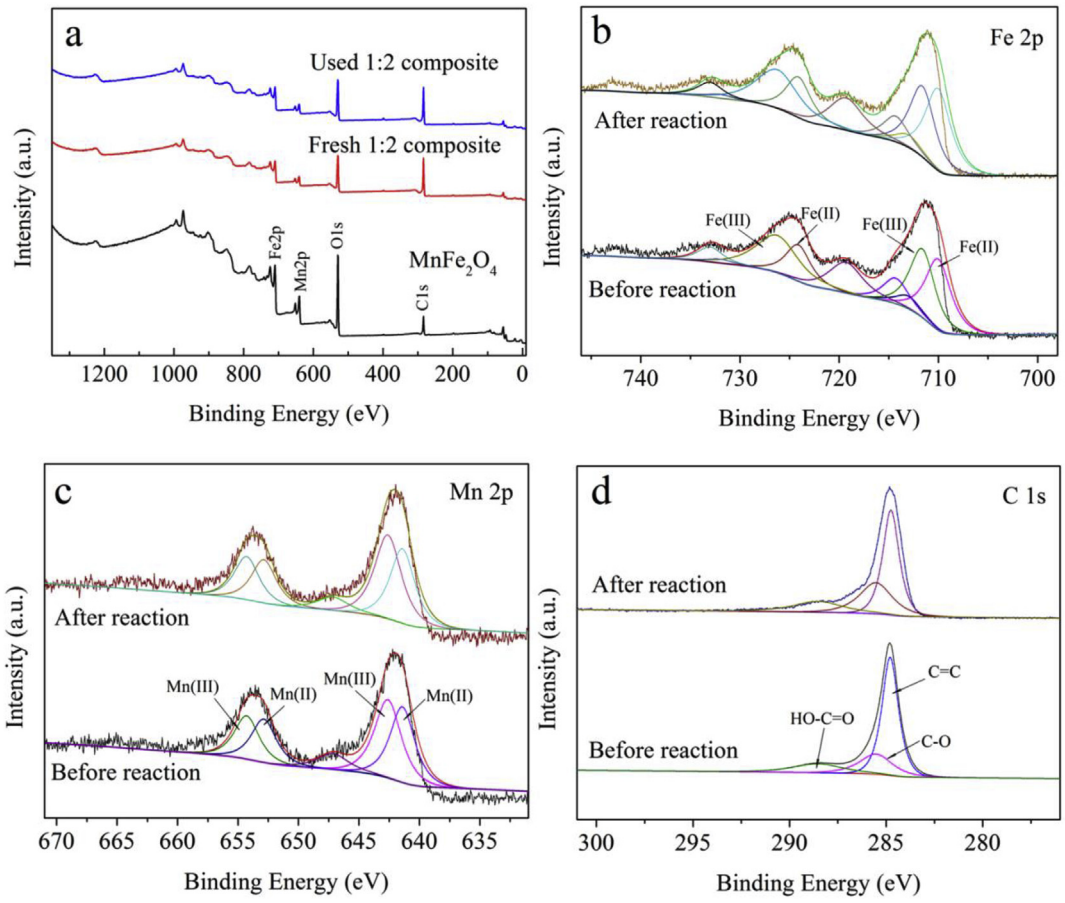

Fig. 6. XPS spectra of survey (a) of bare $MnFe_2O_4$ and $MnFe_2O_4$/bio-char composite with 1:2 mass ratio, Fe 2p (b), Mn 2p (c) and C 1s (d) of $MnFe_2O_4$/bio-char composite with 1:2 mass ratio before and after reaction.

719.30 eV, which indicates the presence of Fe^{3+} cations. The Fe $2p^{3/2}$ with the Eb of 710.96 eV slightly shifted after Fenton-like reaction under visible light irradiation, which means that part of Fe^{3+} has been transformed into Fe^{2+} (Yamashita and Hayes, 2008; Yao et al., 2014; Zhou et al., 2016). So, this phenomenon affirms that Fe takes part in the Fenton reaction process.

In order to explore the effect of Mn in the photo-Fenton reaction process, Mn 2p spectra are shown in Fig. 6c. It was found that two main peaks at 641.97 and 653.52 eV are assigned to Mn $2p^{3/2}$ and Mn $2p^{1/2}$, respectively. A satellite peak at 647.15 eV may be a signal of Mn^{2+}. After reaction with H_2O_2, the satellite peak near 647.15 eV became weaker, this suggests that Mn^{2+} on surface of the catalyst were partially transformed into Mn^{3+} after reaction (Zhou et al., 2016). According to this result, we can verify that the Mn ions play a similar role as Fe ions in the photo-Fenton reaction process (Yao et al., 2014; Zhou et al., 2016). The reaction process could be as follows:

$$Mn^{2+}+H_2O_2 \rightarrow Mn^{3+} + HO^- + {}^{\bullet}OH \quad (9)$$

$$Mn^{3+}+H_2O_2 \rightarrow Mn^{2+} + H^+ + HO_2{}^{\bullet} \quad (10)$$

Mn metal in the magnetite structure strongly accelerates peroxide decomposition in the process of degradation. T.D. Nguyen et al. (2011) reported that Fe_2MnO_4/AC-H has a much higher MO degradation efficiency than Fe_3O_4/AC—H. Besides, $MnFe_2O_4$ nanoparticles have inverse spinel structure, in which Mn^{2+} occupies the octahedral site and Fe^{3+} ions occupy both octahedral and tetrahedral sites. Mn^{2+} ions on the octahedral site exposed to the surface play a significant role in peroxide decomposition (Wei et al., 2017). Besides, according to the result of Costa et al. (2006), the reduction of Mn^{3+} by Fe^{2+} is thermodynamically favorable as shown by the following equations:

$$Fe^{3+}+e^- = Fe^{2+}\ E_0 = 0.77V \quad (11)$$

$$Mn^{3+}+e^- = Mn^{2+}\ E_0 = 1.51V \quad (12)$$

$$Fe^{2+}+Mn^{3+} = Fe^{3+}+ Mn^{2+}\ E_0 = 0.74V \quad (13)$$

The higher reduction potential of Mn^{3+} compared to Fe^{3+} facilitated the reduction of Mn^{3+}, generated Mn^{2+} again take part in the catalytic decomposition until H_2O_2 was consumed. In other ways, the isomorphism substitution of $Mn^{2+}$for Fe^{2+} in magnetite would cause some defects and distortion in magnetite structure due to their different metal ion radius, which leads to the formation of oxygen vacancies. It is known that defects and oxygen vacancies are the active sites and are beneficial for the generation of •OH (Zhong et al., 2012).

The high-resolution XPS spectra of carbon are shown in Fig. 6d. The C 1s spectra can be deconvoluted into three peaks corresponding to C=C (284.8 eV) , C—O(286.7 eV) and HO—C=O (288.5 eV). The highest peak assigned to C=C bonds proves that bio-char has high degree of aromatization which was pyrolyzed under anaerobic condition. The peak of C=C bonds decreased after photo-Fenton reaction and another peak of C—O bonds increased,

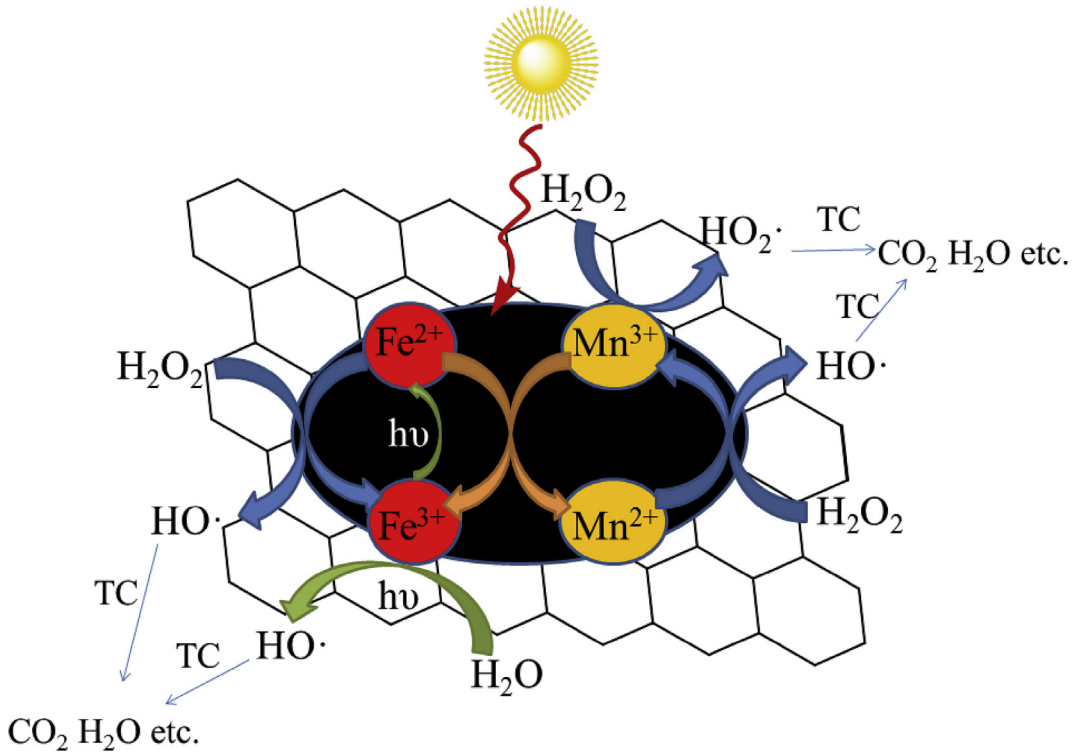

Fig. 7. Possible degradation mechanism diagram of TC by $MnFe_2O_4$/bio-char composite in the presence of H_2O_2 and visible light.

these transformation reveals that surface bio-char are partially oxidized by the active radicals (Zhou et al., 2016). So, this result could also explain that higher bio-char content would suppress catalytic effect of composite by consuming some active radicals rather than oxidizing pollutants.

So, TC degradation mechanism was described in Fig. 7. First, the Mn^{2+} on the surface catalyzed H_2O_2 and generated •OH (eq. (9)). Then Fe^{2+} which was produced by photo-reduction (eq. (3)) was partially oxidized by Mn^{3+} and generated Mn^{2+} and Fe^{3+} (eq. (13)). Besides, we could assume Mn^{3+} can be easily reduced by H_2O_2 in near neutral conditions and consumes a lot of H_2O_2 (eq. (10)), ascribing to the obvious signal of superoxide radical in ESR. Thus, the circulation of Mn (II/III) could decompose H_2O_2 and produce a mass of •OH. On the other hand, some Fe^{2+} could also react with H_2O_2 and generates •OH (eq. (1)). The Fe^{3+} was again photo-reduced leading to the recycle of Fe (II/III). The •OH generated on the surface of catalyst decompose TC into intermediates and further mineralize into inorganic ion and water. As discussed above, some of •OH would oxidize bio-char rather than degrading TC, resulting in inefficient consumption.

3.9. The stability and application in various wastewaters

The recyclability of the catalyst is significant in practical application. Therefore, in order to explore the catalytic stability of $MnFe_2O_4$/bio-char composite in Fenton process, the catalysts were recovered to run a cycle experiment. From Fig. S10, the degradation efficiency of four cycles was 95%, 94%, 92%, 90%, respectively. And leaching of metal ions after each cycles were below 0.2 mg L^{-1}, which accounts for very little compared with total metal content. Besides, structural transformation of catalyst has been tested in Fig. S11. As we can see from the XRD pattern of the catalysts before and after reaction, there is almost no change in XRD pattern before and after reaction, indicating the stability of the catalysts. The combination of spinel structure of $MnFe_2O_4$ and stable bio-char matrix guarantee promising structural stability. Most importantly, we can recover the catalyst by a convenient and efficient way, in which the catalyst was separated by an exterior magnetic field.

As is well-known, the actual water body is much more complex than simulated wastewater in laboratory. The actual wastewater contains various types of inorganic ions and organic matters, which could influence the catalytic performance of catalyst towards targeted contaminant (TC). So, in this work, the degradation efficiency of TC by 1:2 composite/H_2O_2 with the assistance of visible light was preliminarily investigated using tap water (Changsha Running-water Company) and river water (taken from Xiangjiang River, changsha). The results are shown in Fig. S12; the degradation process was slightly different in ultra-pure water, tap water and river water system, proving the interference effect of different water quality between these systems. But removal efficiencies towards TC are all around 90% in ultra-pure water, tap water and river water system, which provides a great potential to treat actual wastewater. It's worth noting that all of these three systems can work efficiently without adjusting pH, which indicates extensive applicability in practical situation.

4. Conclusion

In this study, an economic and efficient $MnFe_2O_4$/bio-char composite was synthesized and its catalytic performance was tested through the degradation of TC. The catalytic performance showed that $MnFe_2O_4$/bio-char composite obtained higher catalytic activity in TC degradation than pure $MnFe_2O_4$, which highlights the importance of bio-char. Most important of all, $MnFe_2O_4$/bio-char composite can work efficiently in neutral pH conditions as well as stability and reusability on the elimination of TC. By analyzing the reaction mechanism, both Mn and Fe on the surface of catalyst take part in the decomposition of H_2O_2 and produce •OH.

Considering its magnetic property, stability, reusability and high activity, $MnFe_2O_4$/bio-char composite will have wide application prospect for degradation of antibiotics and organic contaminants.

Acknowledgement

This study was financially supported by the Program for the National Natural Science Foundation of China (51779090, 51408206, 51709101, 51579098, 51521006, 41601272), Science and Technology Plan Project of Hunan Province (2017SK2243), the National Program for Support of Top–Notch Young Professionals of China (2014), the Program for New Century Excellent Talents in University (NCET-13-0186), the Program for Changjiang Scholars and Innovative Research Team in University (IRT-13R17), and Hunan Provincial Science and Technology Plan Project (No. 2016RS3026), the Fundamental Research Funds for the Central Universities (531107050978, 531107051080).

Appendix A. Supplementary data

Supplementary data to this article can be found online at https://doi.org/10.1016/j.chemosphere.2019.02.193.

References

Chen, W.R., Huang, C.H., 2011. Transformation kinetics and pathways of tetracycline antibiotics with manganese oxide. Environ. Pollut. 159, 1092–1100.
Chen, Y.-Y., Ma, Y.-L., Yang, J., Wang, L.-Q., Lv, J.-M., Ren, C.-J., 2017. Aqueous tetracycline degradation by H_2O_2 alone: removal and transformation pathway. Chem. Eng. J. 307, 15–23.
Cheng, M., Lai, C., Liu, Y., Zeng, G., Huang, D., Zhang, C., Qin, L., Hu, L., Zhou, C., Xiong, W., 2018a. Metal-organic frameworks for highly efficient heterogeneous Fenton-like catalysis. Coord. Chem. Rev. 368, 80–92.
Cheng, M., Zeng, G., Huang, D., Lai, C., Liu, Y., Xu, P., Zhang, C., Wan, J., Hu, L., Xiong, W., Zhou, C., 2017. Salicylic acid–methanol modified steel converter slag as heterogeneous Fenton-like catalyst for enhanced degradation of alachlor. Chem. Eng. J. 327, 686–693.
Cheng, M., Zeng, G., Huang, D., Lai, C., Liu, Y., Zhang, C., Wan, J., Hu, L., Zhou, C., Xiong, W., 2018b. Efficient degradation of sulfamethazine in simulated and real wastewater at slightly basic pH values using Co-SAM-SCS/H_2O_2 Fenton-like system. Water Res. 138, 7–18.
Cheng, M., Zeng, G., Huang, D., Lai, C., Xu, P., Zhang, C., Liu, Y., Wan, J., Gong, X., Zhu, Y., 2016. Degradation of atrazine by a novel Fenton-like process and assessment the influence on the treated soil. J. Hazard. Mater. 312, 184–191.
Costa, R.C.C., Lelis, M.F.F., Oliveira, L.C.A., Fabris, J.D., Ardisson, J.D., Rios, R.R.V.A., Silva, C.N., Lago, R.M., 2006. Novel active heterogeneous Fenton system based on $Fe_{3-x}M_xO_4$ (Fe, Co, Mn, Ni): the role of M^{2+} species on the reactivity towards H_2O_2 reactions. J. Hazard. Mater. 129, 171–178.
Dong, H., Zhang, C., Hou, K., Cheng, Y., Deng, J., Jiang, Z., Tang, L., Zeng, G., 2017. Removal of trichloroethylene by biochar supported nanoscale zero-valent iron in aqueous solution. Separ. Purif. Technol. 188, 188–196.
Duan, L., Wang, Z., Hou, Y., Wang, Z., Gao, G., Chen, W., Alvarez, P.J.J., 2016. The oxidation capacity of Mn_3O_4 nanoparticles is significantly enhanced by anchoring them onto reduced graphene oxide to facilitate regeneration of surface-associated Mn(III). Water Res. 103, 101–108.
Feng, J., Hu, X., Yue, P.L., Zhu, H.Y., Lu, G.Q., 2003. A novel laponite clay-based Fe nanocomposite and its photo-catalytic activity in photo-assisted degradation of Orange II. Chem. Eng. Sci. 58, 679–685.
Galindo, R., Menendez, N., Crespo, P., Velasco, V., Bomati-Miguel, O., Díaz-Fernández, D., Herrasti, P., 2014. Comparison of different methodologies for obtaining nickel nanoferrites. J. Magn. Magn. Mater. 361, 118–125.
Goodarz Naseri, M., Saion, E.B., Ahangar, H.A., Hashim, M., Shaari, A.H., 2011. Synthesis and characterization of manganese ferrite nanoparticles by thermal treatment method. J. Magn. Magn. Mater. 323, 1745–1749.
Guo, X., Wang, K., Li, D., Qin, J., 2017. Heterogeneous photo-Fenton processes using graphite carbon coating hollow $CuFe_2O_4$ spheres for the degradation of methylene blue. Appl. Surf. Sci. 420, 792–801.
Hou, L., Wang, L., Royer, S., Zhang, H., 2016. Ultrasound-assisted heterogeneous Fenton-like degradation of tetracycline over a magnetite catalyst. J. Hazard. Mater. 302, 458–467.
Huang, D., Deng, R., Wan, J., Zeng, G., Xue, W., Wen, X., Zhou, C., Hu, L., Liu, X., Xu, P., Guo, X., Ren, X., 2018. Remediation of lead-contaminated sediment by biochar-supported nano-chlorapatite: accompanied with the change of available phosphorus and organic matters. J. Hazard. Mater. 348, 109–116.
Huang, D., Luo, H., Zhang, C., Zeng, G., Lai, C., Cheng, M., Wang, R., Deng, R., Xue, W., Gong, X., Guo, X., Li, T., 2019. Nonnegligible role of biomass types and its compositions on the formation of persistent free radicals in biochar: insight into the influences on Fenton-like process. Chem. Eng. J. 361, 353–363.
Iurascu, B., Siminiceanu, I., Vione, D., Vicente, M.A., Gil, A., 2009. Phenol degradation in water through a heterogeneous photo-Fenton process catalyzed by Fe-treated laponite. Water Res. 43, 1313–1322.
Ji, Y., Shi, Y., Dong, W., Wen, X., Jiang, M., Lu, J., 2016. Thermo-activated persulfate oxidation system for tetracycline antibiotics degradation in aqueous solution. Chem. Eng. J. 298, 225–233.
Jiang, X., Li, L., Cui, Y., Cui, F., 2017. New branch on old tree: green-synthesized RGO/Fe_3O_4 composite as a photo-Fenton catalyst for rapid decomposition of methylene blue. Ceram. Int. 43, 14361–14368.
Jinisha, R., Gandhimathi, R., Ramesh, S.T., Nidheesh, P.V., Velmathi, S., 2018. Removal of Rhodamine B dye from aqueous solution by electro-Fenton process using iron-doped mesoporous silica as a heterogeneous catalyst. Chemosphere 200, 446–454.
Juang, R.-S., Yei, Y.-C., Liao, C.-S., Lin, K.-S., Lu, H.-C., Wang, S.-F., Sun, A.-C., 2018. Synthesis of magnetic Fe_3O_4/activated carbon nanocomposites with high surface area as recoverable adsorbents. J. Taiwan Inst. Chem. Eng. 90, 51–60.
Lai, C., Wang, M.-M., Zeng, G.-M., Liu, Y.-G., Huang, D.-L., Zhang, C., Wang, R.-Z., Xu, P., Cheng, M., Huang, C., Wu, H.-P., Qin, L., 2016. Synthesis of surface molecular imprinted TiO_2/graphene photocatalyst and its highly efficient photocatalytic degradation of target pollutant under visible light irradiation. Appl. Surf. Sci. 390, 368–376.
Lai, C., Zhang, M., Li, B., Huang, D., Zeng, G., Qin, L., Liu, X., Yi, H., Cheng, M., Li, L., Chen, Z., Chen, L., 2019. Fabrication of CuS/$BiVO_4$ (040) binary heterojunction photocatalysts with enhanced photocatalytic activity for Ciprofloxacin degradation and mechanism insight. Chem. Eng. J. 358, 891–902.
Li, B., Lai, C., Zeng, G., Qin, L., Yi, H., Huang, D., Zhou, C., Liu, X., Cheng, M., Xu, P., Zhang, C., Huang, F., Liu, S., 2018. Facile hydrothermal synthesis of Z-scheme $Bi_2Fe_4O_9$/Bi_2WO_6 heterojunction photocatalyst with enhanced visible light photocatalytic activity. ACS Appl. Mater. Interfaces. 10, 18824–18836.
Li, Y., Qu, J., Gao, F., Lv, S., Shi, L., He, C., Sun, J., 2015. In situ fabrication of Mn_3O_4 decorated graphene oxide as a synergistic catalyst for degradation of methylene blue. Appl. Catal., B 162, 268–274.
Liu, B., Tian, L., Wang, R., Yang, J., Guan, R., Chen, X., 2017. Pyrrolic-N-doped graphene oxide/Fe_2O_3 mesocrystal nanocomposite: efficient charge transfer and enhanced photo-Fenton catalytic activity. Appl. Surf. Sci. 422, 607–615.
Liu, X., Zhou, Y., Zhang, J., Luo, L., Yang, Y., Huang, H., Peng, H., Tang, L., Mu, Y., 2018. Insight into electro-Fenton and photo-Fenton for the degradation of antibiotics: mechanism study and research gaps. Chem. Eng. J. 347, 379–397.
Mazarío, E., Mayoral, A., Salas, E., Menéndez, N., Herrasti, P., Sánchez-Marcos, J., 2016. Synthesis and characterization of manganese ferrite nanoparticles obtained by electrochemical/chemical method. Mater. Des. 111, 646–650.
Mazilu, I., Ciotonea, C., Chirieac, A., Dragoi, B., Catrinescu, C., Ungureanu, A., Petit, S., Royer, S., Dumitriu, E., 2017. Synthesis of highly dispersed iron species within mesoporous (Al-)SBA-15 silica as efficient heterogeneous Fenton-type catalysts. Microporous Mesoporous Mater. 241, 326–337.
Nguyen, T.D., Phan, N.H., Do, M.H., Ngo, K.T., 2011. Magnetic Fe_2MO_4 (M: Fe, Mn) activated carbons: fabrication, characterization and heterogeneous Fenton oxidation of methyl orange. J. Hazard. Mater. 185, 653–661.
Nogueira, R.F., Oliveira, M.C., Paterlini, W.C., 2005. Simple and fast spectrophotometric determination of H_2O_2 in photo-Fenton reactions using metavanadate. Talanta 66, 86–91.
Ouyang, D., Yan, J., Qian, L., Chen, Y., Han, L., Su, A., Zhang, W., Ni, H., Chen, M., 2017. Degradation of 1,4-dioxane by biochar supported nano magnetite particles activating persulfate. Chemosphere 184, 609–617.
Qian, X., Ren, M., Fang, M., Kan, M., Yue, D., Bian, Z., Li, H., Jia, J., Zhao, Y., 2018. Hydrophilic mesoporous carbon as iron(III)/(II) electron shuttle for visible light enhanced Fenton-like degradation of organic pollutants. Appl. Catal., B 231, 108–114.
Qin, L., Zeng, G., Lai, C., Huang, D., Zhang, C., Xu, P., Hu, T., Liu, X., Cheng, M., Liu, Y., Hu, L., Zhou, Y., 2017. A visual application of gold nanoparticles: simple, reliable and sensitive detection of kanamycin based on hydrogen-bonding recognition. Sensor. Actuator. B Chem. 243, 946–954.
Rusevova, K., Kopinke, F.-D., Georgi, A., 2012. Nano-sized magnetic iron oxides as catalysts for heterogeneous Fenton-like reactions—influence of Fe(II)/Fe(III) ratio on catalytic performance. J. Hazard. Mater. 241–242, 433–440.
Son, E.B., Poo, K.M., Chang, J.S., Chae, K.J., 2018. Heavy metal removal from aqueous solutions using engineered magnetic biochars derived from waste marine macro-algal biomass. Sci. Total Environ. 615, 161–168.
Timofeeva, M.N., Khankhasaeva, S.T., Talsi, E.P., Panchenko, V.N., Golovin, A.V., Dashinamzhilova, E.T., Tsybulya, S.V., 2009. The effect of Fe/Cu ratio in the synthesis of mixed Fe, Cu, Al-clays used as catalysts in phenol peroxide oxidation. Appl. Catal., B 90, 618–627.
Tongaree, S., Flanagan, D.R., Poust, R.I., 1999. The Effects of pH and mixed solvent systems on the solubility of oxytetracycline. Pharmaceut. Dev. Technol. 4, 571–580.
Tuček, J., Kemp, K.C., Kim, K.S., Zboril, R., 2014. Iron-oxide-supported nanocarbon in lithium-ion batteries, medical, catalytic, and environmental applications. ACS Nano 8, 7571–7612.
Ueda Yamaguchi, N., Bergamasco, R., Hamoudi, S., 2016. Magnetic $MnFe_2O_4$–graphene hybrid composite for efficient removal of glyphosate from water. Chem. Eng. J. 295, 391–402.
Villegas- Guzman, P., Giannakis, S., Rtimi, S., Grandjean, D., Bensimon, M., de Alencastro, L.F., Torres-Palma, R., Pulgarin, C., 2017. A green solar photo-Fenton process for the elimination of bacteria and micropollutants in municipal

wastewater treatment using mineral iron and natural organic acids. Appl. Catal., B 219, 538–549.
Wan, Z., Wang, J., 2017. Degradation of sulfamethazine using Fe_3O_4-Mn_3O_4/reduced graphene oxide hybrid as Fenton-like catalyst. J. Hazard. Mater. 324, 653–664.
Wang, H., Wu, Y., Feng, M., Tu, W., Xiao, T., Xiong, T., Ang, H., Yuan, X., Chew, J.W., 2018a. Visible-light-driven removal of tetracycline antibiotics and reclamation of hydrogen energy from natural water matrices and wastewater by polymeric carbon nitride foam. Water Res. 144, 215–225.
Wang, H., Wu, Y., Xiao, T., Yuan, X., Zeng, G., Tu, W., Wu, S., Lee, H.Y., Tan, Y.Z., Chew, J.W., 2018b. Formation of quasi-core-shell In_2S_3/anatase TiO_2@metallic $Ti_3C_2T_x$ hybrids with favorable charge transfer channels for excellent visible-light-photocatalytic performance. Appl. Catal., B 233, 213–225.
Wang, H., Wu, Y., Yuan, X., Zeng, G., Zhou, J., Wang, X., Chew, J.W., 2018c. Clay-inspired MXene-based electrochemical devices and photo-electrocatalyst: state-of-the-art progresses and challenges. Adv. Mater. 30 (12), 1704561.
Wang, J., Liu, C., Li, J., Luo, R., Hu, X., Sun, X., Shen, J., Han, W., Wang, L., 2017. In-situ incorporation of iron-copper bimetallic particles in electrospun carbon nanofibers as an efficient Fenton catalyst. Appl. Catal., B 207, 316–325.
Wang, J.L., Xu, L.J., 2012. Advanced oxidation processes for wastewater treatment: formation of hydroxyl radical and application. Crit. Rev. Environ. Sci. Technol. 42, 251–325.
Wang, R.-Z., Huang, D.-L., Liu, Y.-G., Zhang, C., Lai, C., Zeng, G.-M., Cheng, M., Gong, X.-M., Wan, J., Luo, H., 2018d. Investigating the adsorption behavior and the relative distribution of Cd^{2+} sorption mechanisms on biochars by different feedstock. Bioresour. Technol. 261, 265–271.
Wei, C., Feng, Z., Scherer, G.G., Barber, J., Shao-Horn, Y., Xu, Z.J., 2017. Cations in octahedral sites: a descriptor for oxygen electrocatalysis on transition-metal spinels. Adv. Mater. 29, 1606800.
Xiao, H., Liu, R., Zhao, X., Qu, J., 2008. Enhanced degradation of 2,4-dinitrotoluene by ozonation in the presence of manganese(II) and oxalic acid. J. Mol. Catal. Chem. 286, 149–155.
Xiong, W., Tong, J., Yang, Z., Zeng, G., Zhou, Y., Wang, D., Song, P., Xu, R., Zhang, C., Cheng, M., 2017. Adsorption of phosphate from aqueous solution using iron-zirconium modified activated carbon nanofiber: Performance and mechanism. J. Colloid Interf. Sci. 493, 17–23.
Xu, H.Y., Prasad, M., Liu, Y., 2009. Schorl: a novel catalyst in mineral-catalyzed Fenton-like system for dyeing wastewater discoloration. J. Hazard. Mater. 165, 1186–1192.
Yamashita, T., Hayes, P., 2008. Analysis of XPS spectra of Fe^{2+} and Fe^{3+} ions in oxide materials. Appl. Surf. Sci. 254, 2441–2449.
Yan, J., Han, L., Gao, W., Xue, S., Chen, M., 2015. Biochar supported nanoscale zerovalent iron composite used as persulfate activator for removing trichloroethylene. Bioresour. Technol. 175, 269–274.
Yao, Y., Cai, Y., Lu, F., Wei, F., Wang, X., Wang, S., 2014. Magnetic recoverable $MnFe_2O_4$ and $MnFe_2O_4$-graphene hybrid as heterogeneous catalysts of peroxymonosulfate activation for efficient degradation of aqueous organic pollutants. J. Hazard. Mater. 270, 61–70.
Yi, H., Huang, D., Qin, L., Zeng, G., Lai, C., Cheng, M., Ye, S., Song, B., Ren, X., Guo, X., 2018. Selective prepared carbon nanomaterials for advanced photocatalytic application in environmental pollutant treatment and hydrogen production. Appl. Catal., B 239, 408–424.
Zhang, J., Wang, H., Yuan, X., Zeng, G., Tu, W., Wang, S., 2019. Tailored indium sulfide-based materials for solar-energy conversion and utilization. J. Photochem. Photobiol. C. 38, 1–26.
Zhang, Y., Boyd, S.A., Teppen, B.J., Tiedje, J.M., Li, H., 2014. Organic acids enhance bioavailability of tetracycline in water to Escherichia coli for uptake and expression of antibiotic resistance. Water Res. 65, 98–106.
Zhang, Z., Gao, P., Cheng, J., Liu, G., Zhang, X., Feng, Y., 2018. Enhancing anaerobic digestion and methane production of tetracycline wastewater in EGSB reactor with GAC/NZVI mediator. Water Res. 136, 54–63.
Zhong, Y., Liang, X., Zhong, Y., Zhu, J., Zhu, S., Yuan, P., He, H., Zhang, J., 2012. Heterogeneous UV/Fenton degradation of TBBPA catalyzed by titanomagnetite: catalyst characterization, performance and degradation products. Water Res. 46, 4633–4644.
Zhou, G., Wang, D.-W., Yin, L.-C., Li, N., Li, F., Cheng, H.-M., 2012. Oxygen bridges between NiO nanosheets and graphene for improvement of lithium storage. ACS Nano 6, 3214–3223.
Zhou, X., Lai, C., Huang, D., Zeng, G., Chen, L., Qin, L., Xu, P., Cheng, M., Huang, C., Zhang, C., Zhou, C., 2018. Preparation of water-compatible molecularly imprinted thiol-functionalized activated titanium dioxide: selective adsorption and efficient photodegradation of 2, 4-dinitrophenol in aqueous solution. J. Hazard. Mater. 346, 113–123.
Zhou, Y., Xiao, B., Liu, S.-Q., Meng, Z., Chen, Z.-G., Zou, C.-Y., Liu, C.-B., Chen, F., Zhou, X., 2016. Photo-Fenton degradation of ammonia via a manganese–iron double-active component catalyst of graphene–manganese ferrite under visible light. Chem. Eng. J. 283, 266–275.
Zubir, N.A., Yacou, C., Motuzas, J., Zhang, X., Diniz da Costa, J.C., 2014. Structural and functional investigation of graphene oxide-Fe_3O_4 nanocomposites for the heterogeneous Fenton-like reaction. Sci. Rep. 4, 4594.